

Milestone Report for Fiscal Year 2015

M3CA-14-ID-BSU_-0704-017

Yanliang Zhang

Darryl Butt

Vivek Agarwal

July 2015



The INL is a U.S. Department of Energy National Laboratory
operated by Battelle Energy Alliance

DISCLAIMER

This information was prepared as an account of work sponsored by an agency of the U.S. Government. Neither the U.S. Government nor any agency thereof, nor any of their employees, makes any warranty, expressed or implied, or assumes any legal liability or responsibility for the accuracy, completeness, or usefulness, of any information, apparatus, product, or process disclosed, or represents that its use would not infringe privately owned rights. References herein to any specific commercial product, process, or service by trade name, trade mark, manufacturer, or otherwise, does not necessarily constitute or imply its endorsement, recommendation, or favoring by the U.S. Government or any agency thereof. The views and opinions of authors expressed herein do not necessarily state or reflect those of the U.S. Government or any agency thereof.

Yanliang Zhang
Boise State University

Darryl Butt
Boise State University

Vivek Agarwal
Idaho National Laboratory

July 2015

Prepared for the
U.S. Department of Energy
Office of Nuclear Energy
Under DOE Idaho Operations Office
Contract DE-NE0008255

ABSTRACT

The goal of the Nuclear Energy Enabling Technology Research Project is to develop efficient and reliable thermoelectric (TE) generators for self-powered wireless sensor nodes (WSNs) for nuclear applications. The power harvesting technology has crosscutting significance to all United States Department of Energy Office of Nuclear Energy research and development programs, as it will enable self-powered WSNs in multiple nuclear reactor designs and spent fuel storage facilities using thermal energy available in a nuclear power plant or spent fuel storage facility. This project will address the technology gap that exists in realizing truly WSNs due to the need for cables to connect to external power supplies and develop TE power harvesting devices to deliver sufficient power to drive the WSNs. The outcomes of the project will lead to significant advancement in sensors and instrumentation technology, reducing cost, improving monitoring reliability, and therefore enhancing safety. The self-powered WSNs could support the long-term safe and economical operation of all reactor designs and fuel cycle concepts, as well as spent fuel storage and many other nuclear science and engineering applications.

A collaborative team of researchers from Idaho National Laboratory, Boise State University, and the University of Houston performs this project. This partnership brings together expertise and resources encompassing three aspects critical to the success of the project—TEs, nuclear science, and wireless sensors.

The research is based on recent breakthroughs in high-performance nanostructured bulk (nanobulk) TE materials that enable high-efficiency direct heat-to-electricity conversion over a wide temperature range. The nanobulk TE materials that the research team at Boise State University and University of Houston has already developed yield up to a 50% increase in the TE figure of merit, ZT , compared with state-of-the-art bulk counterparts.

This report focuses on the selection of optimal TE materials for this project. The project team has extensively studied two TE material systems—half-Heusler and bismuth telluride materials. This report contains the research results on the TE materials fabrication, characterization, and property measurements.

CONTENTS

ABSTRACT	vii
ACRONYMS	xiv
1. INTRODUCTION	1
2. THERMOELECTRIC MATERIALS FABRICATION AND CHARACTERIZATION.....	2
2.1 Half-Heusler Materials.....	5
2.1.1 Fabrication.....	6
2.1.2 Characterization	7
2.2 Bismuth Telluride Materials.....	11
2.2.1 Fabrication.....	11
2.2.2 Characterization	12
3. THERMOELECTRIC PROPERTY MEASUREMENTS	16
3.1 Half-Heusler Materials.....	16
3.2 Bismuth Telluride Materials.....	21
4. CONCLUSIONS AND FUTURE WORK	24
5. REFERENCES	25

FIGURES

Figure 1. Schematic of self-powered wireless sensor node using thermoelectric generator.....	1
Figure 2. Possible mechanisms of phonon scattering. Atomic defects can scatter short-wavelength phonons whereas nanoinclusions are more effective for scattering mid- or long-wavelength phonons. Grain boundaries are shown scattering phonons. (Illustration taken from Radousky and Liang [5].)	3
Figure 3. Thermoelectric figure of merit, ZT, for many thermoelectric materials reaches empirical maximum as function of temperature, as shown here for many state-of-the-art alloys. Dashed lines show maximum ZT values for bulk state-of-the-art materials; solid lines show recently reported ZT values, many of which were achieved by nanobulk alloys [4].	4
Figure 4. Dr. Sinter spark plasma sintering system (SPS 515S) at Idaho National Laboratory Center for Advanced Energy Studies in Idaho Falls, Idaho (left); thermal technologies vacuum hot press at Boise State University (right).	5
Figure 5. Primitive unit cell of half-Heusler alloy, shown in bold lines, contains three atoms: A, B, and X. Thermoelectric half-Heuslers typically have early transition metal (IIIB or IVB) or rare-earth element occupying site A, main group element (IVA or VA) occupying X site, and transition metal somewhere between A and X on periodic table occupies B site [7].	6
Figure 6. Generic sintering profile used to consolidate half-Heusler powders using spark plasma sintering system. Temperature profile is shown by orange trace and pressure profile is shown by blue trace. Inset shows typical pellet (12.7-mm pellet) produced via spark plasma sintering.	6
Figure 7. Scanning electron microscopy images and particle size distribution of p-type half-Heusler powder showing typical morphology of as-received powders from University of Houston. As seen in images, (a) large agglomerates and particles exist, that upon further examination, (b) show primary particles of very fine crystallites. (c) Particle size distribution as measured by laser scattering particle size analysis shows bimodal distribution of particles around 1 and 10 μm and soft agglomerates around 100 μm ; data from three consecutive measurements are shown to emphasize repeatability of technique.....	8
Figure 8. (a) Typical microstructure of pellets formed using current supply of half-Heusler powder show relatively large grains surrounded by finer microstructure. (b) Regions around large grains consist of grains ranging from submicrometer to nearly 10 μm . (c) Elemental maps of region do not show change in composition within larger grains, but do identify included phases and regions of tin segregation.	9
Figure 9. Detailed look at microstructural features observed in cross-section of sintered pellet, also observed in bright spots in Hf elemental map from Figure 8c. From X-ray spectroscopy analysis, Hf-Zr phase exists throughout the pellet. These common inclusions likely arise from inadequate mixing during powder processing.....	9
Figure 10. X-ray diffraction patterns from p- and n-type half-Heusler powders, pellets consolidate from those powders, and pattern from aluminum X-ray diffraction stage that accounts for extra peaks in pellet data.	10
Figure 11. Elemental maps generated from energy dispersive X-ray spectroscopy of consolidated n-type half-Heusler pellet showing segregated regions rich in both tin (left) and	

titanium (right). Similar analysis of precursor powder showed same segregation of Ti-Sn phase, confirming its presence is artifact of production and not of processing.....	11
Figure 12. Spark plasma sintering temperature profile for making pellets (12.5 mm diameter, 3 mm thick) with hold time of 2 minutes at 345°C to allow capping agent to burn off and 5-minute hold time at final sintering temperature (also described in Table 2).	12
Figure 13. Scanning electron microscopy images of as-received powders of composition Bi ₂ Te _{2.7} Se _{0.3} (batch No. N2315H) in (a) as-received state and (b) after sonication for 10 minutes.	13
Figure 14. X-ray diffraction pattern for as-received Bi ₂ Te _{2.7} Se _{0.3} powder. X-ray diffraction pattern suggests powder is primarily Bi ₂ Te _{2.7} Se _{0.3} phase, but an unidentified phase does exist. Future work will be completed to better understand observed phase.	13
Figure 15. Weight loss measurements at 160, 250, and 345°C in tube furnace (argon atmosphere) on powders of composition Bi ₂ Te _{2.7} Se _{0.3} (batch No. N2315H) to better understand capping agent burnout temperature to identify initial sintering profiles.....	14
Figure 16. Scanning electron microscopy images showing microstructure of sintered pellets pressed from powders of composition Bi ₂ Te _{2.7} Se _{0.3} (batch No. N2315H) at four different conditions listed in Table 2.	15
Figure 17. X-ray diffraction pattern for sintered pellets pressed from powders of composition Bi ₂ Te _{2.7} Se _{0.3} (batch No. N2315H) at four different conditions listed in Table 2.....	15
Figure 18. Plot of mass loss (%), heat flow versus temperature for powders of composition Bi ₂ Te _{2.7} Se _{0.3} (batch No. N2315H) to better identify sintering conditions for fabrication of nanobulk materials.	16
Figure 19. Seebeck coefficient α versus temperature for n-type half-Heusler materials.	17
Figure 20. Electrical conductivity σ versus temperature for n-type half-Heusler materials.	17
Figure 21. Thermal conductivity κ versus temperature for n-Type half-Heusler materials.....	18
Figure 22. Energy dispersive X-ray spectroscopy, ZT, versus temperature for n-type half-Heusler materials.....	18
Figure 23. Seebeck coefficient α versus temperature for p-type half-Heusler materials.	19
Figure 24. Electrical conductivity σ versus temperature for p-type half-Heusler materials.	19
Figure 25. Thermal conductivity κ versus temperature for p-type half-Heusler materials.	20
Figure 26. Energy dispersive X-ray spectroscopy, ZT, versus temperature for p-type half-Heusler materials.....	20
Figure 27. Seebeck coefficient α versus temperature for n-type bismuth telluride materials.....	21
Figure 28. Electrical conductivity σ versus temperature for n-type bismuth telluride materials.....	21
Figure 29. Thermal conductivity κ versus temperature for n-type bismuth telluride materials.....	22
Figure 30. Energy dispersive X-ray spectroscopy, ZT, for n-type bismuth telluride materials.....	22
Figure 31. Seebeck coefficient α versus temperature for p-type bismuth telluride materials.....	23
Figure 32. Electrical conductivity σ versus temperature for p-type bismuth telluride materials.....	23
Figure 33. Thermal conductivity κ versus temperature for p-type bismuth telluride materials.....	24
Figure 34. Energy dispersive X-ray spectroscopy, ZT, for p-type bismuth telluride materials.....	24

TABLES

Table 1. Sintering conditions used for spark plasma sintering of half-Heusler powders and resultant density of monolithic samples, as measured using Archimedes techniques.....	7
Table 2. Spark plasma sintering system sintering conditions for fabricating pellets from $\text{Bi}_2\text{Te}_{2.7}\text{Se}_{0.3}$ powders (batch No. N2315H) using temperature profile shown in Figure 12.	12

ACRONYMS

BiTe	bismuth telluride
BSU	Boise State University
HH	half-Heusler
INL	Idaho National Laboratory
NPP	nuclear power plant
SEM	scanning electron microscopy
SPS	spark plasma sintering
SPSS	spark plasma sintering system
TE	thermoelectric
TEG	thermoelectric generator
UH	University of Houston
WSN	wireless sensor node
XRD	X-ray diffraction

Error! Reference source not found.

1. INTRODUCTION

The power harvesting technology has crosscutting significance to all United States Department of Energy Office of Nuclear Energy research and development programs, as it will enable self-powered wireless sensor nodes (WSNs) [1] in multiple nuclear reactor designs and spent fuel storage facilities. While wireless communications enable the elimination of communication wires, a technology gap still exists in realizing truly WSNs due to the need for cables to connect to external power supplies. The Nuclear Energy Enabling Technology Research Project will address this important technology gap and develop thermoelectric (TE) power harvesting devices to deliver sufficient power to drive the WSNs. The benefit of self-powered WSNs goes beyond the cost savings of eliminating the need for cable installation and maintenance. Self-powered WSNs will offer significant expansion in remote monitoring of nuclear facilities by providing important data on nuclear power plant (NPP) equipment and component status during station blackouts or accident conditions, and thus significantly improve reliability and safety in NPPs and spent fuel storage facilities [2].

The project goal is to develop efficient and reliable TE generators (TEGs) based on high-efficiency nanostructured bulk materials that directly convert heat into electricity to power WSNs for nuclear applications. Solid-state power harvesting technologies will play a crucial role in establishing self-powered WSNs for the nuclear industry. Figure 1 shows a schematic of a WSN powered by a TEG that harvests the thermal energy available in an NPP or a spent fuel storage facility. A collaborative team of researchers from Idaho National Laboratory, Boise State University (BSU), and the University of Houston (UH) performs this project. This partnership brings together expertise and resources encompassing three aspects critical to project success—TEs, nuclear science, and wireless sensors.

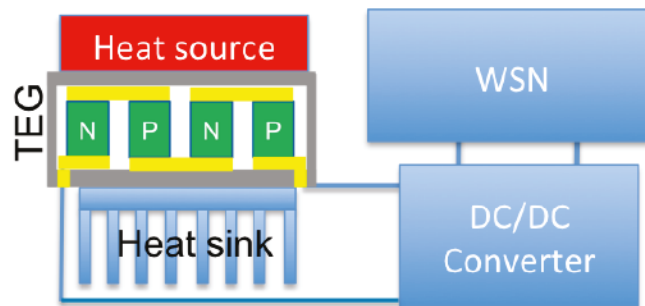


Figure 1. Schematic of self-powered wireless sensor node using thermoelectric generator.

The convergence of high-efficiency nanostructured TE materials and abundant waste heat in a nuclear facility makes TEGs a very promising power harvesting technology. This research is based on breakthroughs in high-performance nanostructured bulk (nanobulk) TE materials that enable high-efficiency direct heat-to-electricity conversion over a wide temperature range. The nanobulk TE materials that the project team at BSU and UH has already developed yield up to a 50% increase in the TE figure of merit, ZT , compared with state-of-the-art bulk counterparts over the temperature range of 30 to 600°C. In this research, the BSU researchers developed TEGs based on nanobulk half-Heusler (HH) and bismuth telluride (BiTe) materials that cover application temperatures from 30 to 600°C. Performance in this temperature range makes these materials excellent candidates for power harvesting for WSNs for nuclear applications.

While TE materials have undergone tremendous advancements in the past two decades through nanostructuring, their applications in nuclear industry largely remain unexploited. This project will utilize two of the most efficient and robust TE material systems—HH and BiTe materials. This project will

significantly advance the knowledge on the properties and performance of nanostructured TE materials under irradiation effect in a nuclear environment, and the expected outcomes will enable reliable power harvesting technology that will realize self-powered WSNs.

This report focuses on the selection of optimal TE materials for this project. The project team extensively studied two TE material systems—HH and BiTe materials. This report contains the research results on the TE materials fabrication, characterization, and property measurements.

2. THERMOELECTRIC MATERIALS FABRICATION AND CHARACTERIZATION

TE materials can realize direct conversions between thermal energy and electricity. The fact that this conversion is made without any moving parts means that TEGs can be quite robust. Furthermore, the high power density and low space requirements make TEGs ideal for self-powered, remote monitoring of NPPs and spent fuel casks. The development of self-powered WSNs can replace the current approaches of facility monitoring while eliminating the need of cable installations and external power sources. Additionally, the temperature range of available waste heat within a nuclear facility must be assessed to properly identify a TE material system and the operating conditions it must endure, including radiation tolerance. When selecting a material system for WSN applications within a nuclear facility, it must be considered if the TEG can generate adequate power within the space allowed; temperature at which the TEG realizes its peak-efficiency is near that of what can be accessed within the nuclear facility; and TEG can operate and survive in the selected environment, most notably temperature and radiation.

Considering the above, the BSU researchers down-selected from many possible TE material systems to focus on only two—BiTe and HH materials. BiTe materials are one of the oldest and most studied TE materials and are widely considered a benchmark TEG [3]. Until just recently, BiTe materials were the best performing TE materials, which resulted in them being the most commercially-available materials in TE and thermal management devices. Since BiTe materials are commercially available, it is logical to study their survivability in the previously described WSN applications.

More recently, higher-temperature and better-efficiency TEGs have been sought and developed. The other material system considered here are HH materials, which are a higher-temperature TE material with comparable power generation to BiTe materials. HH materials are alloys, which form a specific crystal structure. The structure of HH materials can be described as four interpenetrating face-centered-cubic sublattices, three of which are occupied by metallic elements and the fourth being vacant. The relative ability of the metallic elements within the HH structure to interchangeably occupy lattice sites suggests that these alloys will exhibit excellent radiation tolerance while maintaining their TE performance.

In addition, both BiTe and HH materials have been recently fabricated with very fine grain structures in attempts to increase their TE performance, which is also a desirable feature while increasing radiation tolerance. To summarize, these two materials were selected for this project for the following reasons:

- These materials have been extensively studied and their performance is well known in the TE community
- Together, these materials cover a wide range of operating temperatures, making them suitable for various sites around nuclear facilities
- The structure of these alloys has the potential to survive in a radiation environment.

The performance of TE materials is determined by the TE figure of merit, defined as

$$ZT = (\alpha^2 \sigma / \kappa) T$$

where

- α = Seebeck coefficient ($\mu\text{V/K}$)
- σ = electrical conductivity (S/m)
- κ = thermal conductivity (W/mK)
- T = absolute temperature (K).

A good-performing TE material will have a ZT maximized by a high electrical conductivity and a low thermal conductivity. However, the two material properties are inherently coupled (i.e., a good conductor of electricity is typically a good conductor of heat). This is because electricity and heat are carried through a material by the simultaneous flow of electrons and phonons, respectively [4]. A materials engineer can take advantage of the fact that the two species of carrier have different mean-free-paths of travel. By introducing structural features on the scale of the mean-free-path of phonons, one can increase the scattering events of a traveling phonon and suppress a materials thermal conductivity without significantly altering its electrical conductivity. Some possible mechanisms of phonon scattering are shown in Figure 2. As seen in Figure 2, atomic defects can scatter short-wavelength phonons but nanometer-scale inclusions are thought to be more effective for scattering mid- or long-wavelength phonons; grain boundaries are also shown scattering phonons.

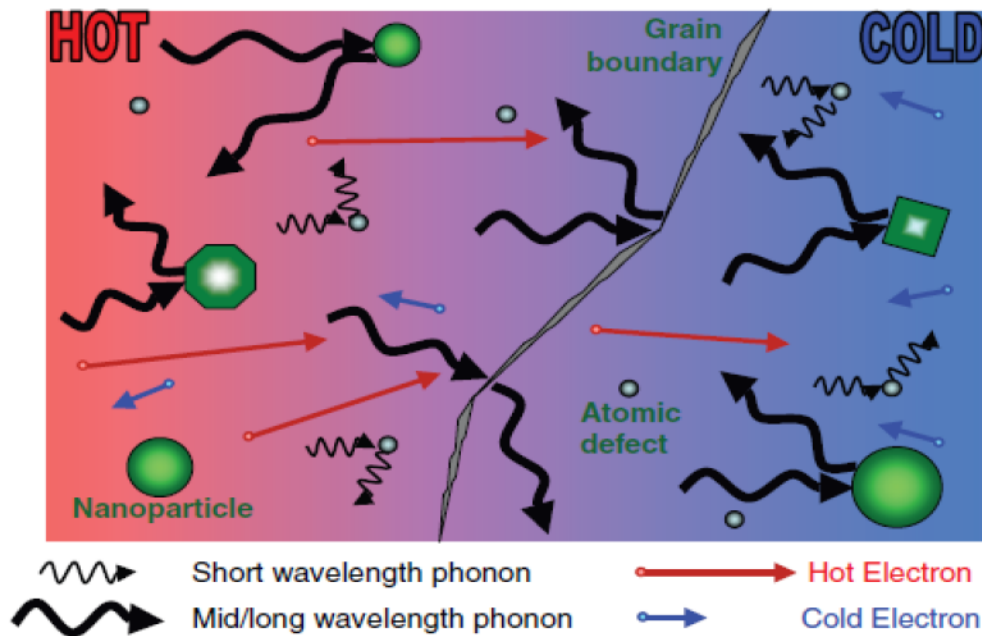


Figure 2. Possible mechanisms of phonon scattering. Atomic defects can scatter short-wavelength phonons whereas nanoinclusions are more effective for scattering mid- or long-wavelength phonons. Grain boundaries are shown scattering phonons. (Illustration taken from Radousky and Liang [5].)

Accordingly, typical materials fabrication considerations to increase the performance, or the ZT , of a potential TE material include:

- Preferentially aligning grains along favorable transport directions
- Reducing grain size to take advantage of favorable interfacial scattering processes

- Introducing grain boundary phases or coated-grains to increase scattering processes
- Embedding nanometer-scale inclusions to increase scattering processes
- Producing laminar or multilayer structures to increase scattering processes.

Using such techniques, Yan et al. [6] demonstrated the increase of the performance of a TE material by focusing on reducing the grain size of the bulk samples. The strategy used by Yan et al.[6] and the strategy adopted by the current research are to pulverize a cast ingot into nanopowder using a high-energy ball mill and sintering the resulting powder. This technique produces a so-called “nanobulk” material and it has been shown to achieve a 60% higher ZT than the cast TE alloy, which contains much larger grains. The results from Minnich et al. [4] illustrated in Figure 3 show the improvements in ZT of some of these nanobulk TE alloys by sintering the nanometer-scaled powders into a dense bulk structure while retaining nanometer-scaled grains. In order to fabricate the optimal TE materials, BSU researchers utilized high-temperature and high-pressure sintering techniques such as inert-atmosphere hot-pressing and field-assisted sintering techniques, namely spark plasma sintering (SPS) (Figure 4). It is believed that the previously demonstrated enhancement in ZT achieved by using a nanometer-scaled structure can be further elevated by maintaining a finer structure during sintering and achieving a smaller distribution of grain sizes.

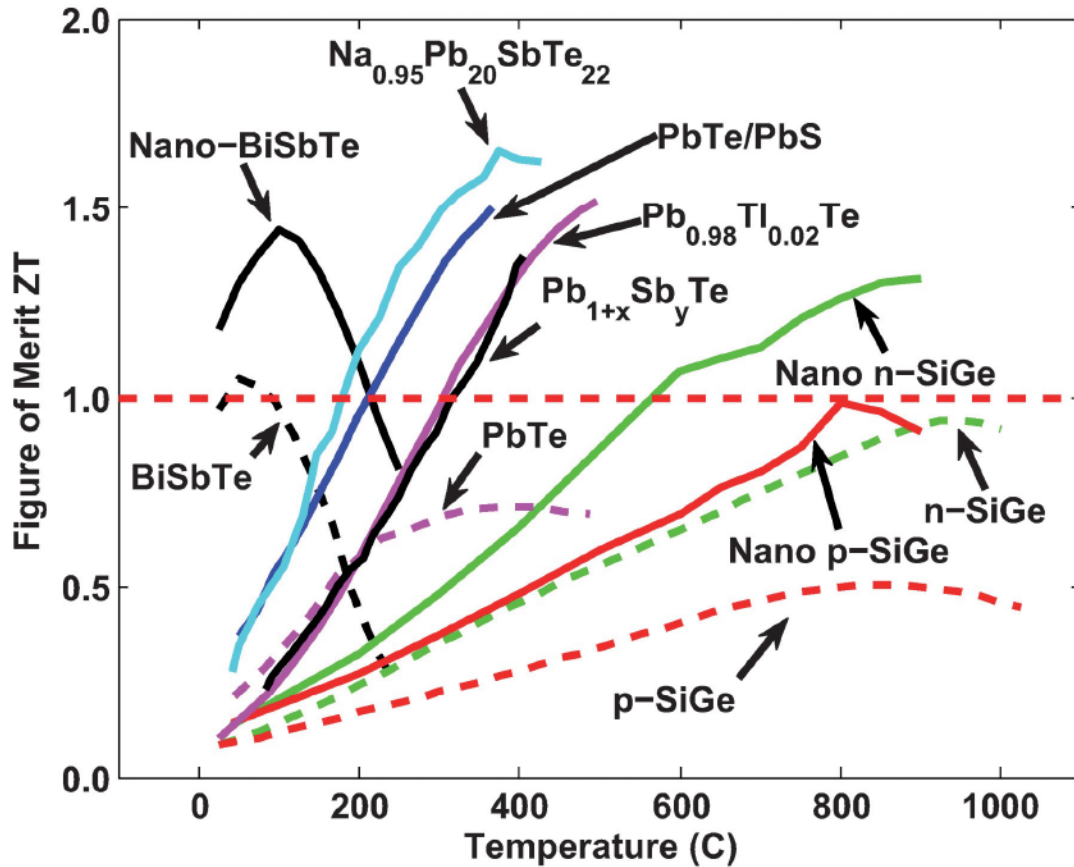


Figure 3. Thermoelectric figure of merit, ZT, for many thermoelectric materials reaches empirical maximum as function of temperature, as shown here for many state-of-the-art alloys. Dashed lines show maximum ZT values for bulk state-of-the-art materials; solid lines show recently reported ZT values, many of which were achieved by nanobulk alloys [4].



Figure 4. Dr. Sinter spark plasma sintering system (SPS 515S) at Idaho National Laboratory Center for Advanced Energy Studies in Idaho Falls, Idaho (left); thermal technologies vacuum hot press at Boise State University (right).

2.1 Half-Heusler Materials

The HH crystal structure, shown in Figure 5, can be thought of as four interpenetrating face centered cubic sublattices, three of which are occupied by metallic elements and fourth being vacant, or as a rock-salt structure with only one of two body-diagonal sites occupied. The primitive unit cell, shown in bold lines in Figure 5, contains three atoms, A, B, and X. TE HH materials typically have an early transition metal (IIIB or IVB) or a rare-earth element occupying site A, a main group element (IVA or VA) occupying the X site, and a transition metal somewhere between A and X on the periodic table occupies the B site. For HH material to be a good TE material it should be a narrow band-gap semiconductor and have a total of 18 valence electrons within a primitive unit cell. Of the more than 100 HH compounds identified by Yang et al. [7] there are nearly 30 that should possess good TE properties. Among the 30 HH compounds, a few have attracted much more interest than others because of the relative abundance and low toxicity of their constituents; these being the HfNiSn- and ZrCoSb-based systems.

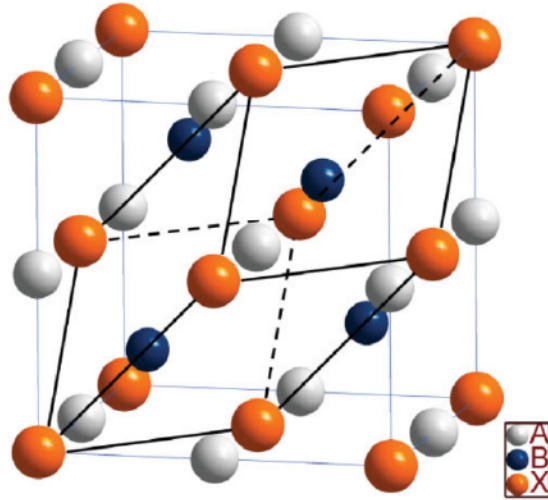


Figure 5. Primitive unit cell of half-Heusler alloy, shown in bold lines, contains three atoms: A, B, and X. Thermoelectric half-Heuslers typically have early transition metal (IIIB or IVB) or rare-earth element occupying site A, main group element (IVA or VA) occupying X site, and transition metal somewhere between A and X on periodic table occupies B site [7].

2.1.1 Fabrication

The BSU researchers successfully consolidated nanobulk HH powders using an inert-atmosphere hot press and powders provided by GMZ Energy on a prior project in 2014. The results were promising since the properties of the synthesized nanobulk samples were comparable to those consolidated by GMZ Energy using their “direct current hot-press,” which is very similar to a commercial SPSS system (SPSS). Therefore, upon receiving HH nanopowders for the current study, the SPSS located at the INL Center for Advanced Energy Studies in Idaho Falls, Idaho, was used for pellet fabrication. The generic sintering profile shown in Figure 6 was used to press all HH pellets in the SPSS but detailed sintering parameters (temperature, time duration, and pressure) at different stages of the heating profile were systematically changed to optimize the microstructure and mechanical integrity of the sintered product.

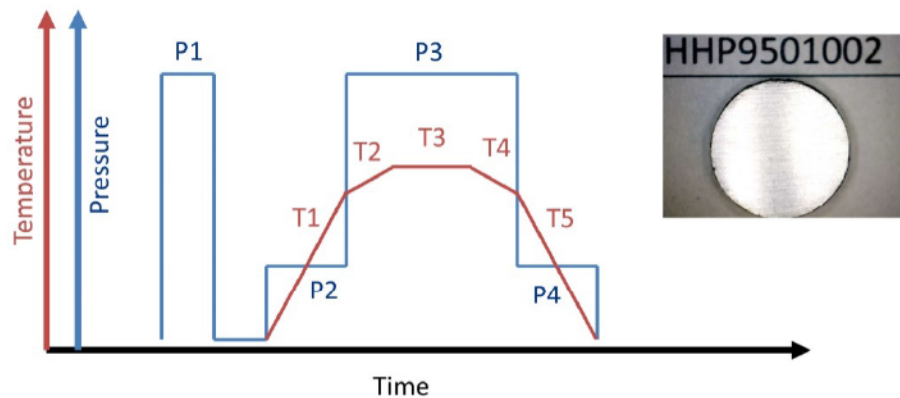


Figure 6. Generic sintering profile used to consolidate half-Heusler powders using spark plasma sintering system. Temperature profile is shown by orange trace and pressure profile is shown by blue trace. Inset shows typical pellet (12.7-mm pellet) produced via spark plasma sintering.

The sintering process was started by loading the provided HH powders into graphite dies in an argon-atmosphere glovebox to prevent oxidation. The graphite die was lined with graphite foil and the powder was pressed using a hydraulic pellet press (P1) prior to sintering. The SPSS requires a minimum pressure (P2) to maintain contact between the die and the equipment's rams before an electric current can be applied. An initial rapid heating rate (T1) is used to decrease the time the samples are exposed to high temperatures to decrease grain growth. At higher temperature close to the sintering temperature (T2), the maximum pressure is applied (P3) to assist in particle compaction. It should be noted that the slower temperature ramp during this time is to allow for particle rearrangement and reduce residual stresses in the monolithic sample. The maximum pressure is maintained throughout the maximum temperature dwell (T3). An initially slow cooling rate (T4) is employed to prevent thermal shock that has been seen to crack the monolithic sample upon cooling. At this time, the applied pressure is returned to its minimum (P4) to allow the sintered part to contract to its desired size without external geometric restrictions and the part cools to ambient temperature (T5). These sintering parameters were chosen based on prior experience with the SPSS and HH materials. Altogether, six pellets (three n-type pellets and three p-type pellets) were consolidated with the SPSS using the conditions described in Table 1. The pressure and temperature events shown in Table 1 correspond to the generic sintering profile shown in Figure 6. These pellets will provide material for TE performance measurements, device fabrication and testing, and material for future irradiation studies.

Table 1. Sintering conditions used for spark plasma sintering of half-Heusler powders and resultant density of monolithic samples, as measured using Archimedes techniques.

Sample Identification	Pressure Event (MPa)				Temperature Event (°C)					Density (%TD)
	P1	P2	P3	P4	T1	T2	T3	T4	T5	
HHP950802	80	30	80	30	200/min to 650	50/min to 950	950 for 2 min	50/min to 650	80/min to ambient	95.2
HHP9508021										94.5
HHP9501002	100	100			200/min to 950		950 for 2 min	50/min to 150	80/min to ambient	95.2
HHN900802	80	30	80	30	200/min to 600	50/min to 900	900 for 2 min	50/min to 600	80/min to ambient	93.8
HHN9008021										91.0
HHN9001002	100	100			200/min to 900		900 for 2 min	50/min to 150	80/min to ambient	90.9

2.1.2 Characterization

The current study focused on the UH-provided HH powders of the n- and p-type compositions (n-type: $\text{Hf}_{0.5}\text{Ti}_{0.25}\text{Zr}_{0.25}\text{Ni}_{0.99}\text{Sn}_{0.01}$; p-type: $\text{Hf}_{0.5}\text{Zr}_{0.5}\text{CoSb}_{0.8}\text{Sn}_{0.2}$). The powders were fabricated by arc-melting the alloy constituents into a homogenously-mixed ingot followed by high-energy ball milling to reduce particle size. The goal of such procedure is to produce a batch of powder with submicrometer particle size. The morphology of the received powder is shown in

Figure 7a and

Figure 7b. The scanning electron microscopy (SEM) micrographs clearly illustrate that the particle size ranges from slightly submicrometer to tens of micrometers, with agglomerates of near 100 μm (Figure 7a). The visual analysis of particle size agrees with that of particle size analysis conducted at BSU with a Horiba LA-950 laser scattering particle size analyzer. The resulting particle size distribution is shown in

Figure 7c. Closer examination (

Figure 7b) indicates that the primary particles may be comprised of submicrometer sized crystallites, which is a result supported by X-ray diffraction (XRD) and discussed in later sections.

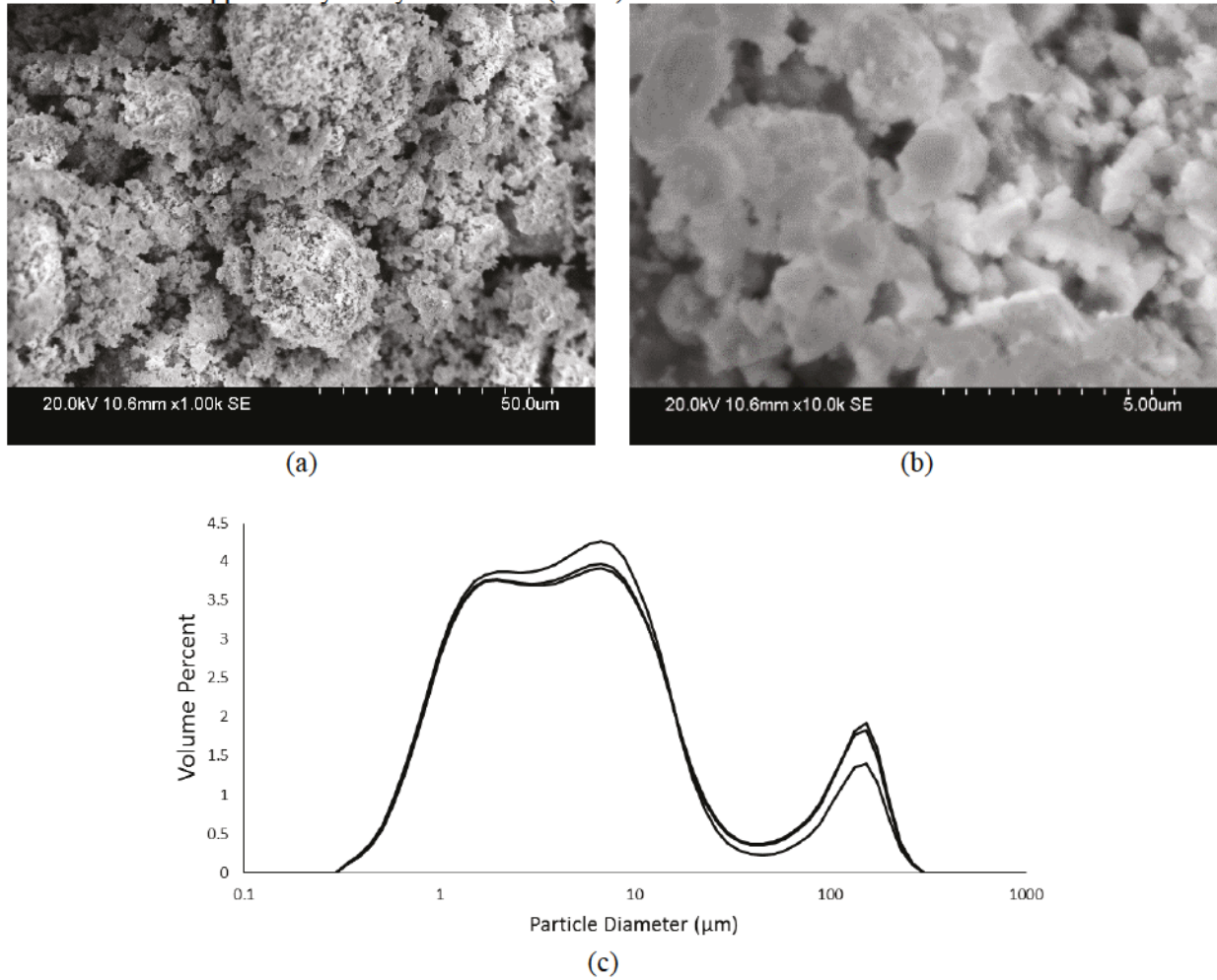


Figure 7. Scanning electron microscopy images and particle size distribution of p-type half-Heusler powder showing typical morphology of as-received powders from University of Houston. As seen in images, (a) large agglomerates and particles exist, that upon further examination, (b) show primary particles of very fine crystallites. (c) Particle size distribution as measured by laser scattering particle size analysis shows bimodal distribution of particles around 1 and 10 μm and soft agglomerates around 100 μm; data from three consecutive measurements are shown to emphasize repeatability of technique.

The consolidated nanobulk materials using these powders result in microstructures with grain sizes ranging from approximately 1 to 10 μm, as shown in Figure 8a. However, as seen in Figure 8b, very large grains exist within the microstructure. Not only can this type of microstructure lead to failure originating from the larger grains, it also is not the desired nanostructured bulk material for maximizing ZT. Further characterization was performed using energy dispersive X-ray spectroscopy at BSU, as shown in Figure 8c. From this analysis, the presence of several phases within a sintered pellet was identified, including a Hf-Zr phase and regions of tin segregation. There is more detail of the Hf-Zr phase in Figure 9. The elemental maps shown in Figure 8c suggest that the large inclusions differ by only their size and not their chemistry. However, the initial materials consolidated so far show TE performance similar to the state-of-the-art materials (further discussed in later sections). It is believed that finer grain sizes can reduce lattice thermal conductivities and realize the full potential of these alloys. Towards that end, BSU

is setting up equipment to cast and mill HH alloys in an effort to have finer control on powder production. The hot press and SPSS will continue to be used to consolidate powders.

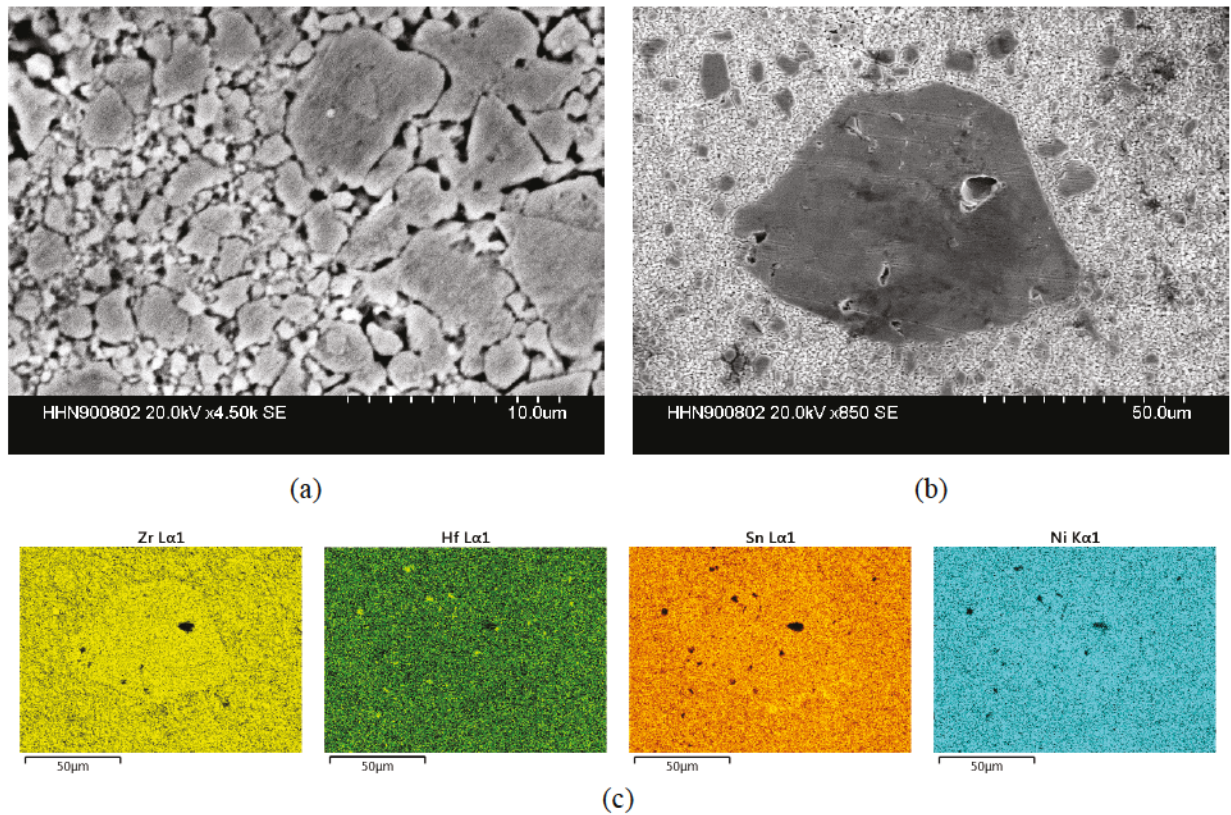


Figure 8. (a) Typical microstructure of pellets formed using current supply of half-Heusler powder show relatively large grains surrounded by finer microstructure. (b) Regions around large grains consist of grains ranging from submicrometer to nearly 10 μm . (c) Elemental maps of region do not show change in composition within larger grains, but do identify included phases and regions of tin segregation.

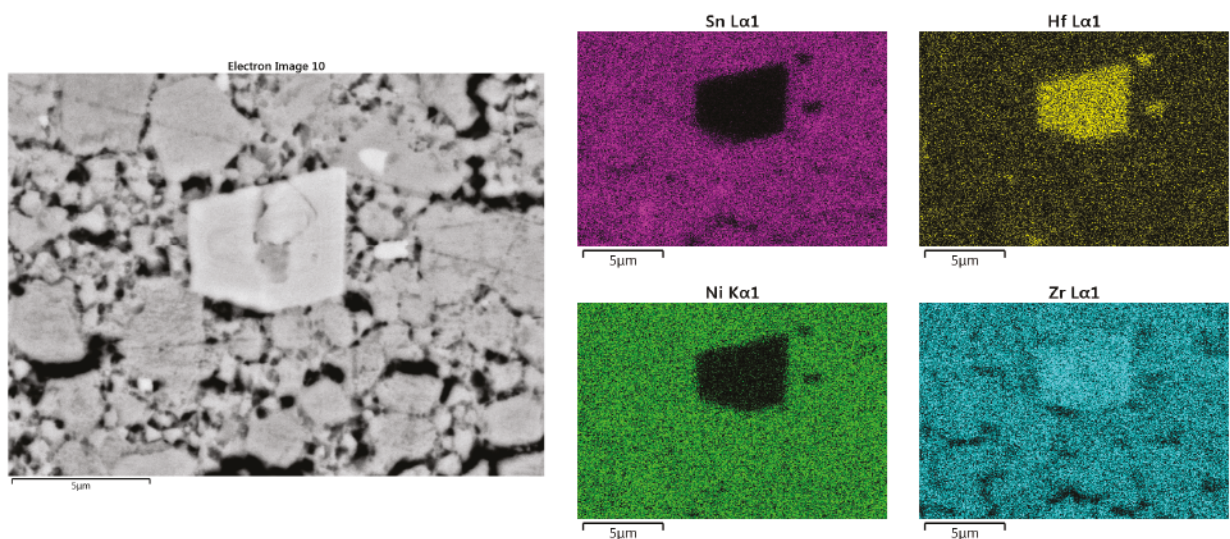


Figure 9. Detailed look at microstructural features observed in cross-section of sintered pellet, also observed in bright spots in Hf elemental map from Figure 8c. From X-ray spectroscopy analysis, Hf-Zr phase exists throughout the pellet. These common inclusions likely arise from inadequate mixing during powder processing.

XRD analysis of received powders and monolithic samples is in good agreement with published diffraction patterns of phase pure HH ingots [6], [7], [8]. The broad diffraction peaks from the powder samples in the XRD pattern presented in Figure 10 suggest a nanometer scaled crystalline powder. The more distinct peaks in the XRD pattern of consolidated pellets, also shown in Figure 10, suggest some grain growth occurred while consolidating pellets from the starting powder. There are no new peaks in the pattern from the pellets that cannot be accounted for by the XRD stage, which is seen at the top of Figure 10. This confirms that no new phases (within the detectable limits of XRD) are created during the sintering process. Although the XRD pattern presented in literature is supposedly phase-pure, the project team believes there are minor phases beyond the detectable limits of the XRD. Contradictory literature reports the inevitable formation of a high-temperature Ti-Sn phase when creating these Ti-Ni-Sn HH alloys from a melt [9], which is similar to the observations presented above. It is agreed that this phase is likely detrimental to TE performance but the effects have yet to be quantified. X-ray spectroscopy has identified the presence of this phase, supported by the elemental maps in Figure 11. The evidence presented here supports the fact that these phases are present within the starting material and are not precipitated during the sintering process. Better understanding of these phases and improvements in the production of HH powders could help eliminate their presence in a sintered part and achieve even greater TE performance.

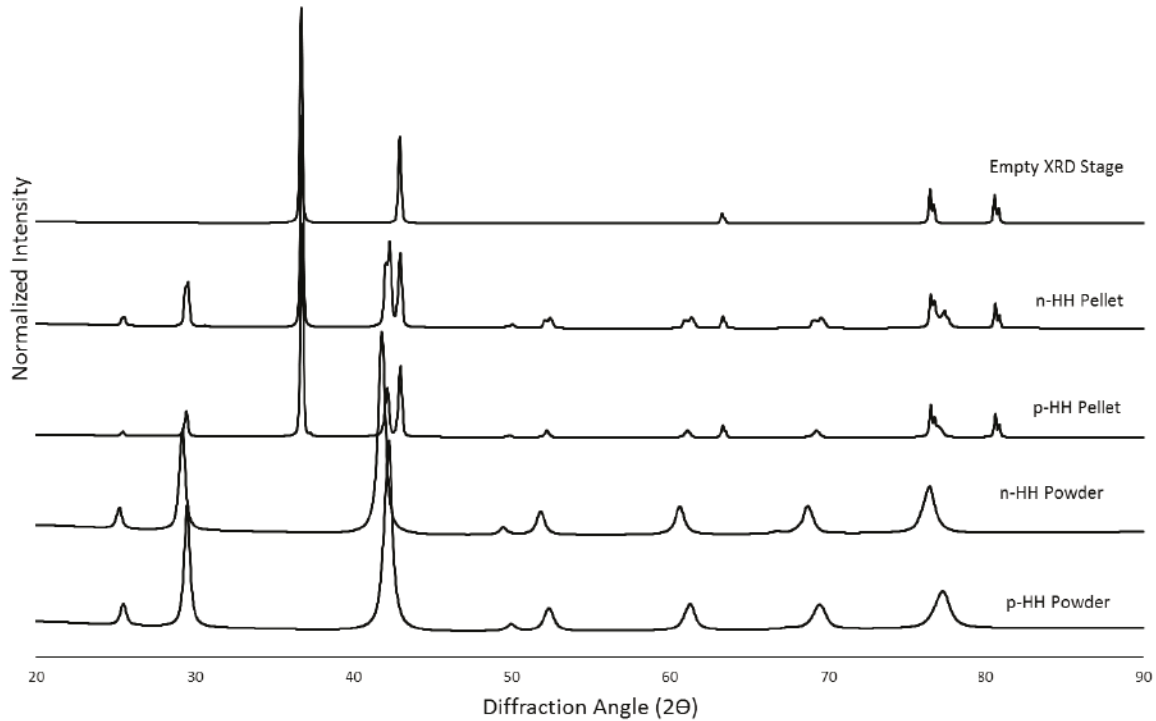


Figure 10. X-ray diffraction patterns from p- and n-type half-Heusler powders, pellets consolidate from those powders, and pattern from aluminum X-ray diffraction stage that accounts for extra peaks in pellet data.

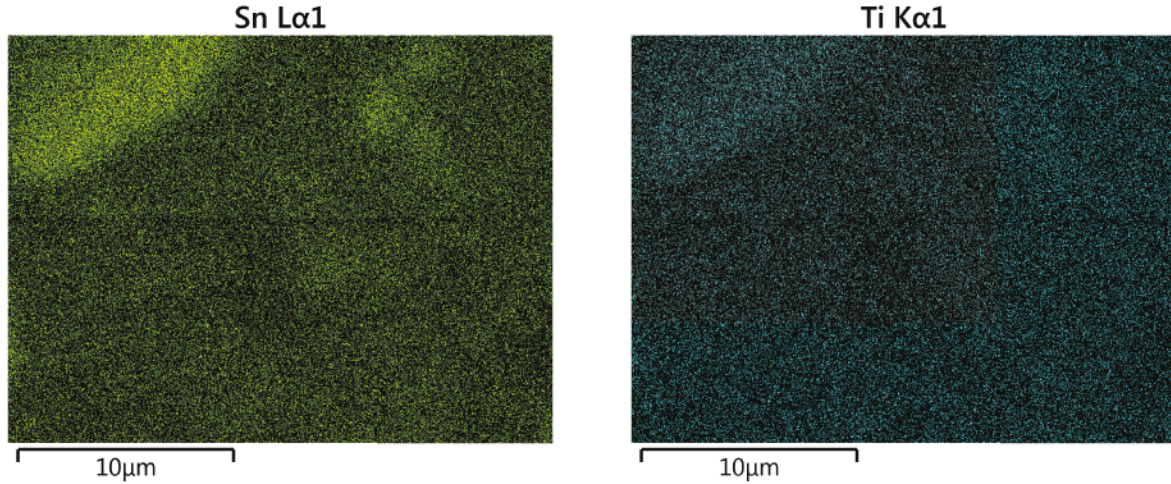


Figure 11. Elemental maps generated from energy dispersive X-ray spectroscopy of consolidated n-type half-Heusler pellet showing segregated regions rich in both tin (left) and titanium (right). Similar analysis of precursor powder showed same segregation of Ti-Sn phase, confirming its presence is artifact of production and not of processing.

2.2 Bismuth Telluride Materials

Bismuth telluride materials are a widely studied and commercially available TE material system. It has been demonstrated that alloying with many different constituents can alter the thermal and electrical transport properties of Bi_2Te_3 materials. It is thought that such an optimization is required to achieve high ZT values (≥ 1) desired for power harvesting within a nuclear facility. Bi_2Te_3 materials have a unique layered structure bonded by Van der Waals forces. Each of the layers consists of five monoatomic sheets (-Te1-Vi-Te2-Bi-Te1-). The Te2 and Te1 atoms in the structure have different charged states that are octahedrally and tetrahedrally coordinated to the neighboring atoms [10]. Additionally, Bi_2Te_3 materials exhibit semiconductor characteristics with a narrow band gap of 0.15 eV and can be alloyed with antimony (Sb) and selenium (Se) to obtain p- and n-type conductors, respectively. This allows the ZT values for such p- and n-type Bi_2Te_3 compositions to increase approximately to 1.5 and 1, respectively.

2.2.1 Fabrication

Similar to the process described above for the consolidation of the HH powders, four pellets (12.5 mm diameter, 3 mm thick) were fabricated using the SPSS at the INL Center for Advanced Energy Studies using four different conditions in order to gain insight into the effects on microstructure and performance of the monolithic samples. The temperatures and pressures with each sample are listed in Table 2. The typical temperature profile for each of the pellets is shown in Figure 12. An additional step (a 120-second dwell at 345°C) was added to the initial thermal profile to facilitate the burnout of the capping agent. The characterization of these powders followed by pellets fabrication is discussed in the following section.

Table 2. Spark plasma sintering system sintering conditions for fabricating pellets from $\text{Bi}_2\text{Te}_{2.7}\text{Se}_{0.3}$ powders (batch No. N2315H) using temperature profile shown in Figure 12.

Temperature (°C)	Pressure (MPa)	Dwell Time (minutes)
425	44	5
475	44	5
475	60	5
475	80	5

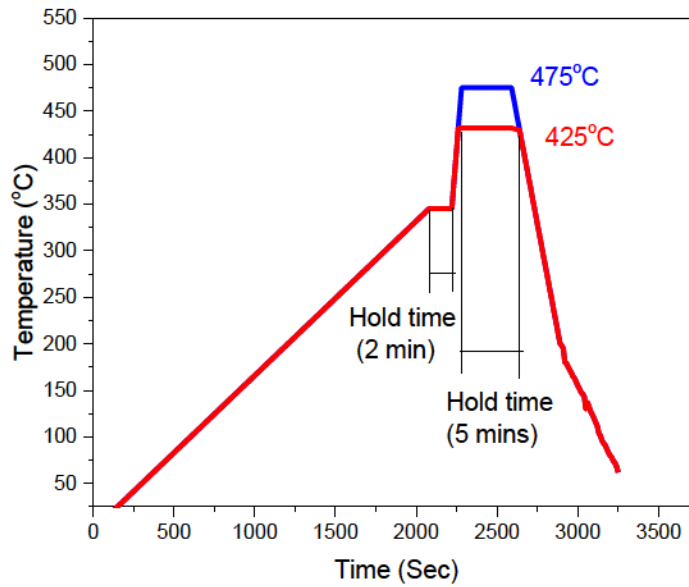


Figure 12. Spark plasma sintering temperature profile for making pellets (12.5 mm diameter, 3 mm thick) with hold time of 2 minutes at 345°C to allow capping agent to burn off and 5-minute hold time at final sintering temperature (also described in Table 2).

2.2.2 Characterization

2.2.2.1 Characterization of Powder. Initial characterization of the powders was performed using SEM and XRD. The SEM image shown in Figure 13 is of the as-received $\text{Bi}_2\text{Te}_{2.7}\text{Se}_{0.3}$ powder (batch No. N2315H) before and after sonication for 10 minutes. Further characterization of this powder is seen in the XRD pattern in Figure 14, which was obtained using a CuK_α x-ray source with a 1.54 Å wavelength. Although the pattern suggests that the powder is primarily $\text{Bi}_2\text{Te}_{2.7}\text{Se}_{0.3}$ phase, there does exist unidentified peaks. Further work will be performed to identify the phases present in the XRD pattern.

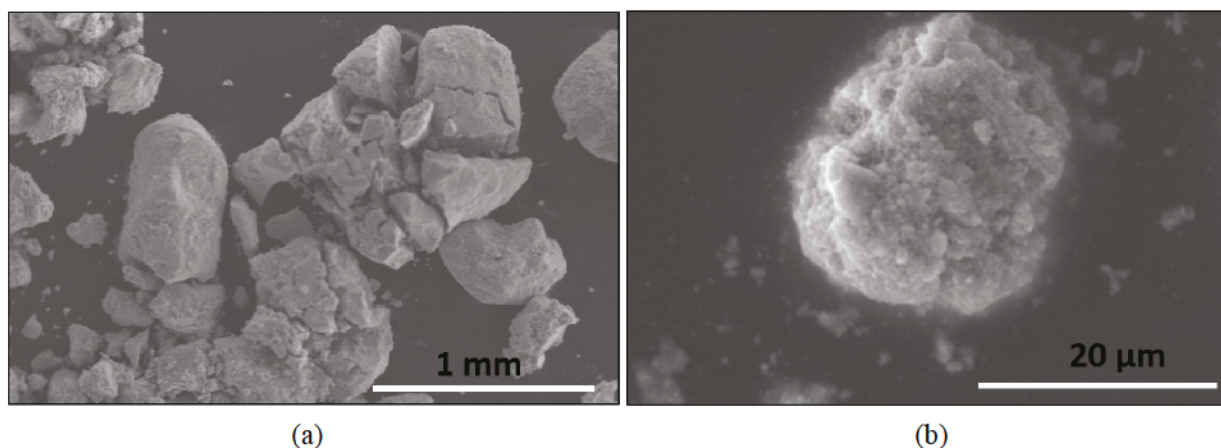


Figure 13. Scanning electron microscopy images of as-received powders of composition $\text{Bi}_2\text{Te}_{2.7}\text{Se}_{0.3}$ (batch No. N2315H) in (a) as-received state and (b) after sonication for 10 minutes.

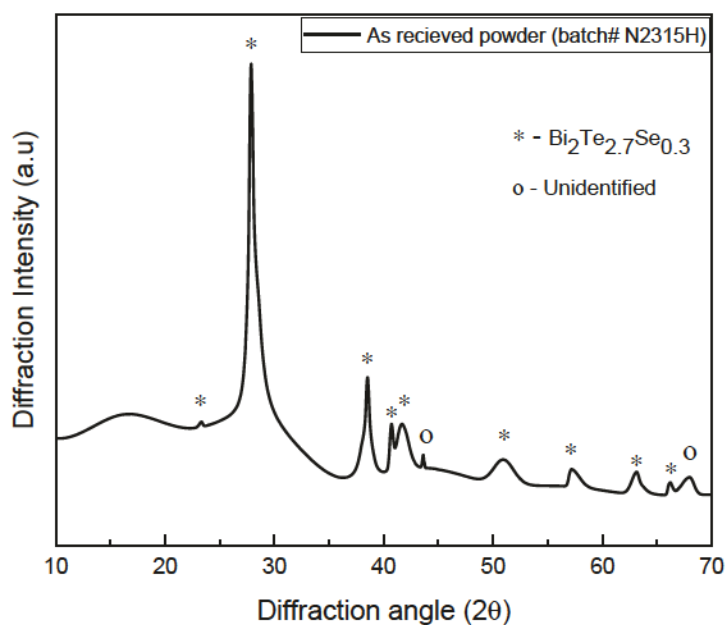


Figure 14. X-ray diffraction pattern for as-received $\text{Bi}_2\text{Te}_{2.7}\text{Se}_{0.3}$ powder. X-ray diffraction pattern suggests powder is primarily $\text{Bi}_2\text{Te}_{2.7}\text{Se}_{0.3}$ phase, but an unidentified phase does exist. Future work will be completed to better understand observed phase.

To better understand the sintering process and gain insight into dwell times and temperatures needed to consolidate these powders (batch No. N2315H), experiments were performed to understand the capping agent burnout process. Accordingly, a weight loss analysis (Figure 15) was completed in a tube furnace with a $10^\circ\text{C}/\text{minute}$ heating rate. The burnout temperature of the capping agent was estimated to be around 345°C .

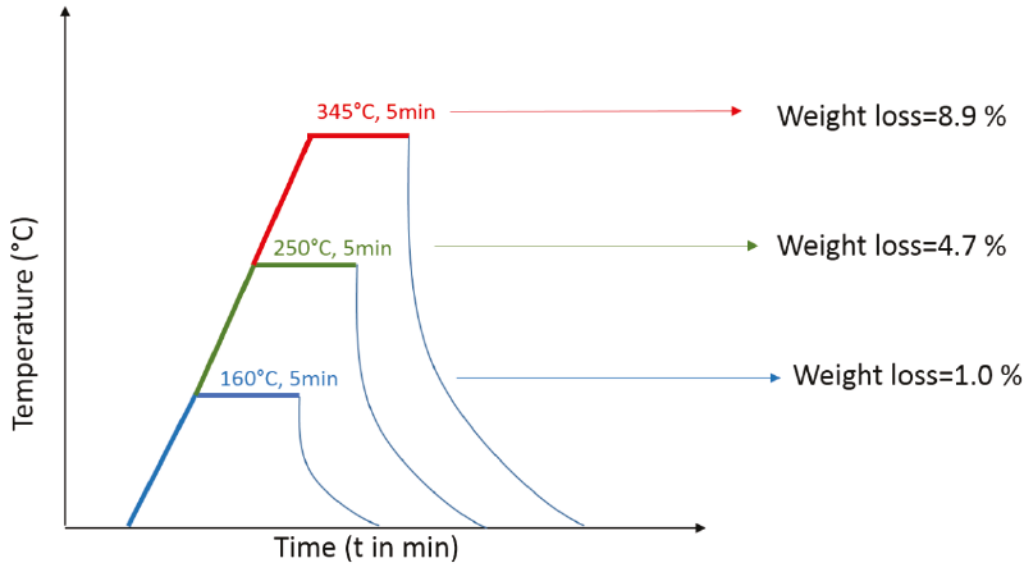


Figure 15. Weight loss measurements at 160, 250, and 345°C in tube furnace (argon atmosphere) on powders of composition $\text{Bi}_2\text{Te}_{2.7}\text{Se}_{0.3}$ (batch No. N2315H) to better understand capping agent burnout temperature to identify initial sintering profiles.

2.2.2.2 Characterization of Sintered Pellets. The density of the sintered pellets was measured using Archimedes' principle and found to be approximately 86% of the theoretical density. To obtain the microstructure, the sintered pellets were polished and etched with 50% concentrated nitric acid. SEM images were obtained for each processing condition (Figure 16). These images indicate dense packing with pores. The sintered pellets have varying grain size. Figure 17 shows XRD patterns obtained for each pellet sintered at four different conditions listed in Table 2. The $\text{Bi}_2\text{Te}_{2.7}\text{Se}_{0.3}$ phase is identified along with a few unidentified peaks, suggesting that there is another phase other than $\text{Bi}_2\text{Te}_{2.7}\text{Se}_{0.3}$. However, a pattern obtained from Sootsman et al. [10] correlates with Figure 17.

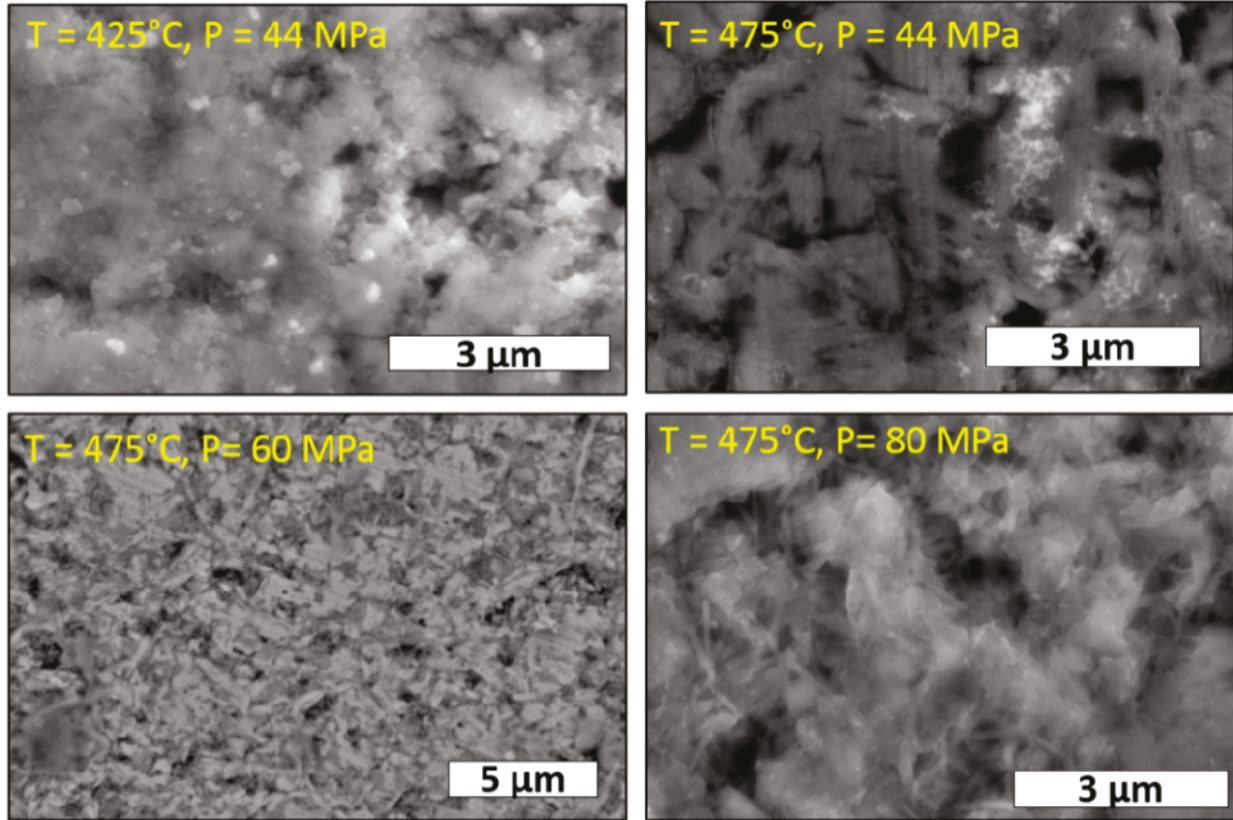


Figure 16. Scanning electron microscopy images showing microstructure of sintered pellets pressed from powders of composition $\text{Bi}_2\text{Te}_{2.7}\text{Se}_{0.3}$ (batch No. N2315H) at four different conditions listed in Table 2.

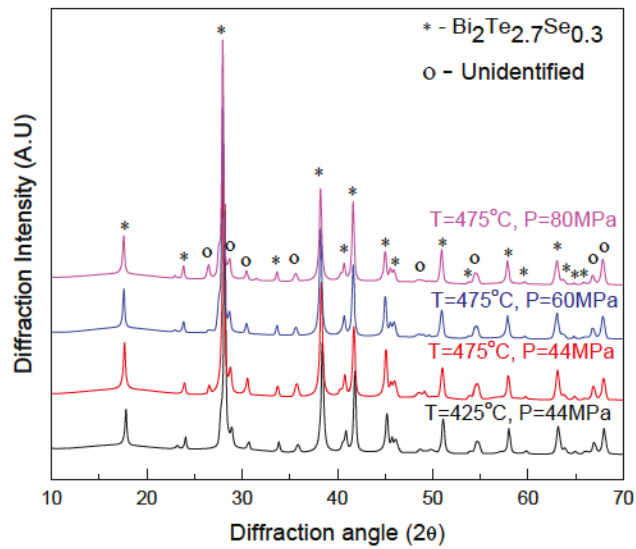


Figure 17. X-ray diffraction pattern for sintered pellets pressed from powders of composition $\text{Bi}_2\text{Te}_{2.7}\text{Se}_{0.3}$ (batch No. N2315H) at four different conditions listed in Table 2.

Since the microstructures of the sintered pellets do not show a desired structure (nanograin), the processing conditions need to be changed. Therefore, to further optimize the SPS condition, thermogravimetric analysis (TGA) was done on the as-received powder (batch No. N2315H). The weight loss and heat flow of the as-received powder (batch No. N2315H) was recorded as a function of temperature. Figure 18 shows a mass loss of 7% (thermogravimetric curve) from 150 to 400°C and also an endothermic reaction is observed at 400°C (heat flow curve). The trend in weight loss obtained in the temperature range of 150 to 345°C by a thermogravimetric curve (Figure 18) is linear, which is similar to that observed in a tube furnace (Figure 15). The endothermic reaction at 400°C can be correlated to the evaporation of the capping agent. Therefore, since thermogravimetric analysis is a better way to anticipate the burnout behavior, it can be concluded that the capping agent is completely eliminated at 400°C.

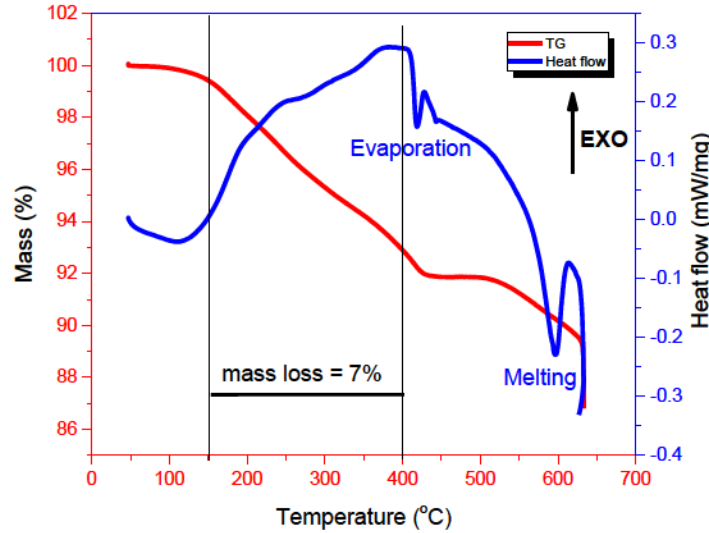


Figure 18. Plot of mass loss (%), heat flow versus temperature for powders of composition $\text{Bi}_2\text{Te}_{2.7}\text{Se}_{0.3}$ (batch No. N2315H) to better identify sintering conditions for fabrication of nanobulk materials.

3. THERMOELECTRIC PROPERTY MEASUREMENTS

The TE properties of the HH and BiTe materials were measured using laser flash analysis to determine thermal diffusivity and Linseis Seebeck resistivity to measure the Seebeck coefficient and electrical conductivity. The density was measured directly and differential scanning calorimetry was used to estimate specific heat, allowing thermal conductivity to be extracted from the thermal diffusivity. Subsections 3.1 and 3.2 provide the following results for the HH and BiTe materials, respectively:

- Seebeck coefficient
- Electrical conductivity
- Thermal conductivity
- Thermoelectric figure of merit ZT.

3.1 Half-Heusler Materials

The TE properties of the HH materials are presented below. In Figures 19 through 26, the blue circles represent materials manufactured at BSU and the red squares represent materials manufactured at UH. Each data point is the mean of three measurements. Error bars representing one standard deviation are too small to see on the scale of these figures.

Figure 19 shows the Seebeck coefficient of the n-type HH materials measured from room temperature to 600°C. The magnitude of the Seebeck coefficient increases from -133 $\mu\text{V/K}$ and -143 $\mu\text{V/K}$ at room temperature for the BSU and UH materials, respectively, to the peak of -187 $\mu\text{V/K}$ and -206 $\mu\text{V/K}$ at about 500°C.

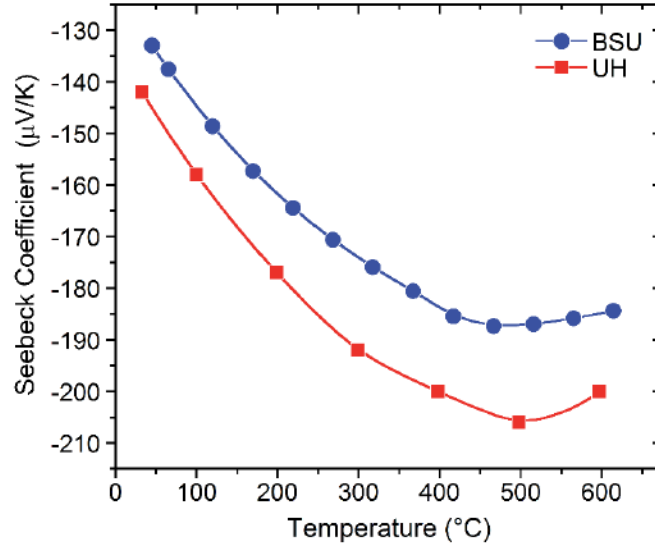


Figure 19. Seebeck coefficient α versus temperature for n-type half-Heusler materials.

Figure 20 shows the electrical conductivity of the n-type HH materials measured from room temperature to 600°C. Conductivity is at a maximum of 160,000 S/m and 150,000 S/m at room temperature for the BSU and UH materials, respectively, and decreases with increasing temperature to a minimum of 107,000 S/m and 103,000 S/m at 600°C.

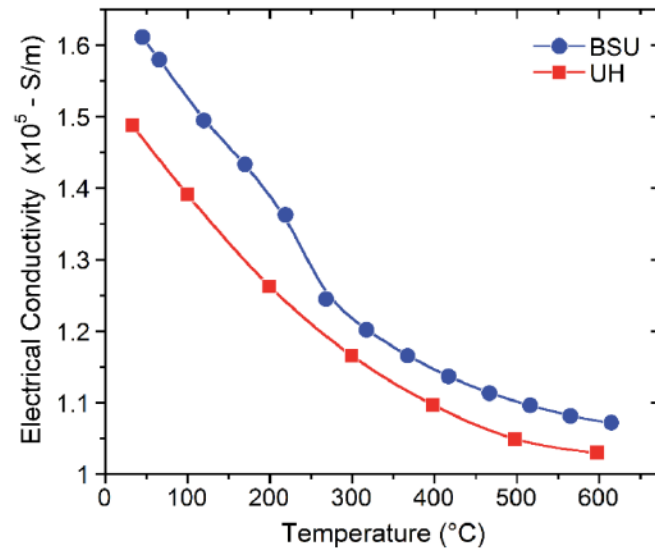


Figure 20. Electrical conductivity σ versus temperature for n-type half-Heusler materials.

Figure 21 shows the thermal conductivity of the n-type HH materials measured from room temperature to 600°C. Conductivity reaches a minimum of 4.0 W/mK and 3.25 W/mK at about 300°C for the BSU and UH materials, respectively.

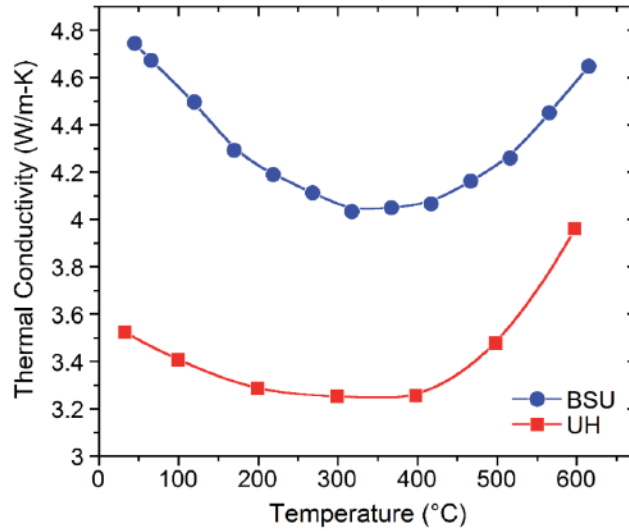


Figure 21. Thermal conductivity κ versus temperature for n-Type half-Heusler materials.

Figure 22 shows the ZT of the n-type HH materials measured from room temperature to 600°C. The BSU materials have peak ZT of 0.71 at 520°C while the UH material has peak ZT of 1.0 at 500°C. This highlights the potential for improvement to the BSU materials through enhanced nanostructuring to reduce thermal conductivity along with optimization of compositions to maximize the Seebeck coefficient and electrical conductivity. Additionally, these data represent BSU's first spark-plasma-sintered materials. Through optimization of pressing conditions such as temperature, pressure, holding times, and ramp rates, all material properties can be improved to reach or exceed those of the best available material.

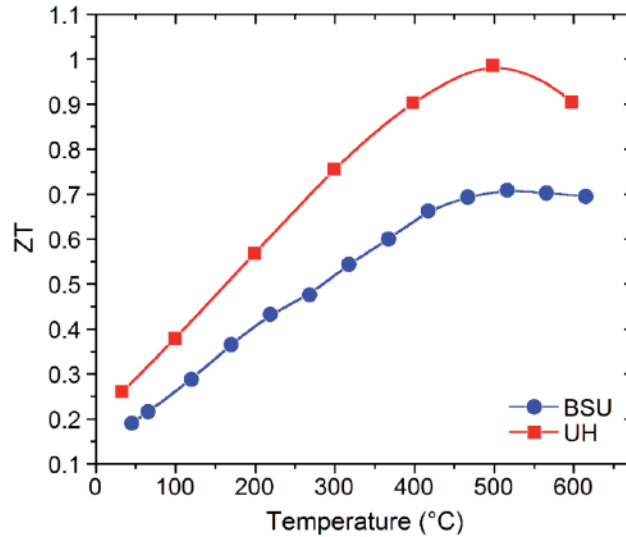


Figure 22. Energy dispersive X-ray spectroscopy, ZT, versus temperature for n-type half-Heusler materials.

Figure 23 shows the Seebeck coefficient of the p-type HH materials measured from room temperature to 600°C. The magnitude of the Seebeck coefficient increases from 150 $\mu\text{V/K}$ and 134 $\mu\text{V/K}$ near room temperature for the BSU and UH materials, respectively, to the peak of 245 $\mu\text{V/K}$ and 216 $\mu\text{V/K}$ at 600°C.

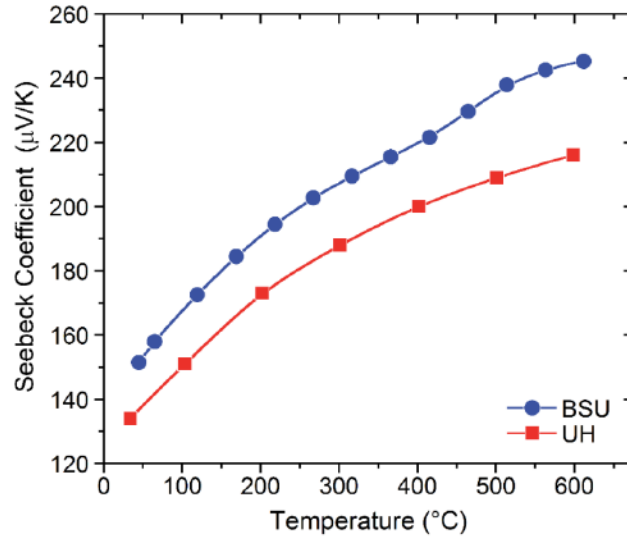


Figure 23. Seebeck coefficient α versus temperature for p-type half-Heusler materials.

Figure 24 shows the electrical conductivity of the p-type HH materials measured from room temperature to 600°C. Conductivity is at a maximum of 60,000 S/m and 93,000 S/m at room temperature for the BSU and UH materials, respectively, and decreases nearly linearly with increasing temperature to a minimum of 43,000 S/m and 58,000 S/m at 600°C.

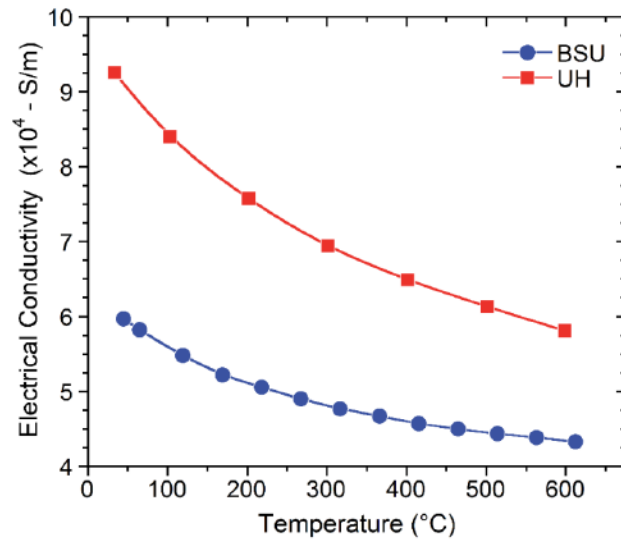


Figure 24. Electrical conductivity σ versus temperature for p-type half-Heusler materials.

Figure 25 shows the thermal conductivity of the p-type HH materials measured from room temperature to 600°C. Conductivity reaches a minimum of about 2.7 W/mK at about 200°C for the BSU materials and 3.0 W/mK at 400°C for the UH materials.

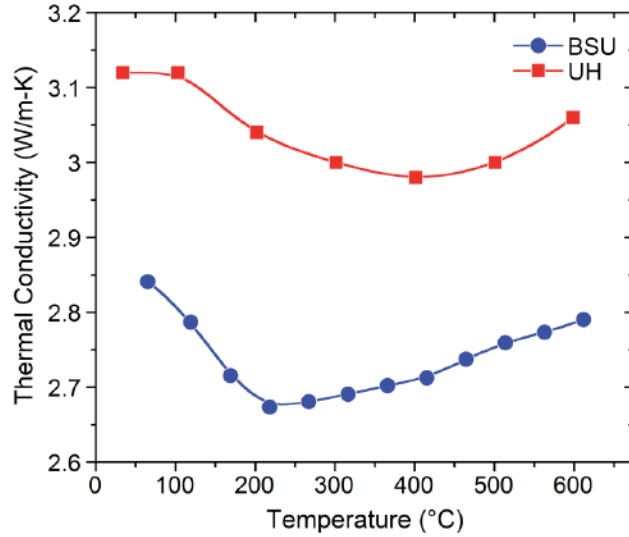


Figure 25. Thermal conductivity κ versus temperature for p-type half-Heusler materials.

Figure 26 shows the ZT of the p-type HH materials measured from room temperature to 600°C. The BSU materials have peak ZT of 0.83 at 610°C while the UH materials have peak ZT of 0.77 at 600°C. Despite exhibiting relatively poor electrical conductivity, the BSU materials are on par with the UH materials due to a higher Seebeck coefficient and lower thermal conductivity. With optimization strategies outlined above for the n-type HH materials, BSU researchers expect to exceed the ZT of the best available p-type HH materials.

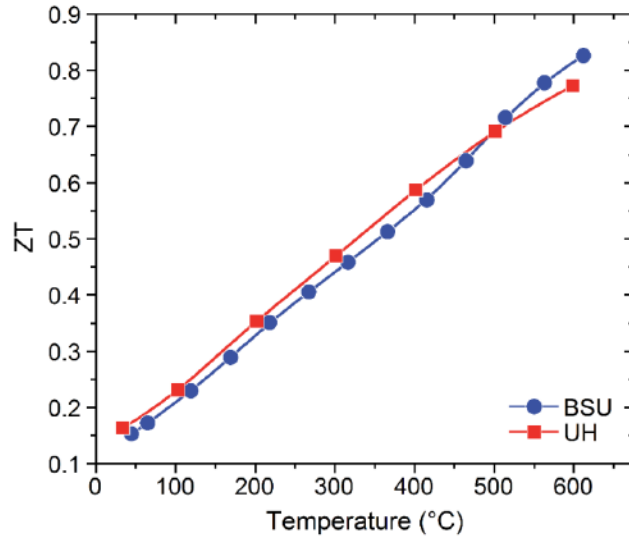


Figure 26. Energy dispersive X-ray spectroscopy, ZT, versus temperature for p-type half-Heusler materials.

3.2 Bismuth Telluride Materials

The TE properties of the BiTe materials manufactured at UH are presented below. BiTe materials are currently in production at BSU.

Figure 27 shows the Seebeck coefficient of the n-type BiTe materials measured from room temperature to 250°C. The magnitude of the Seebeck coefficient increases from $-190 \mu\text{V/K}$ near room temperature to the peak of $-205 \mu\text{V/K}$ at 125°C.

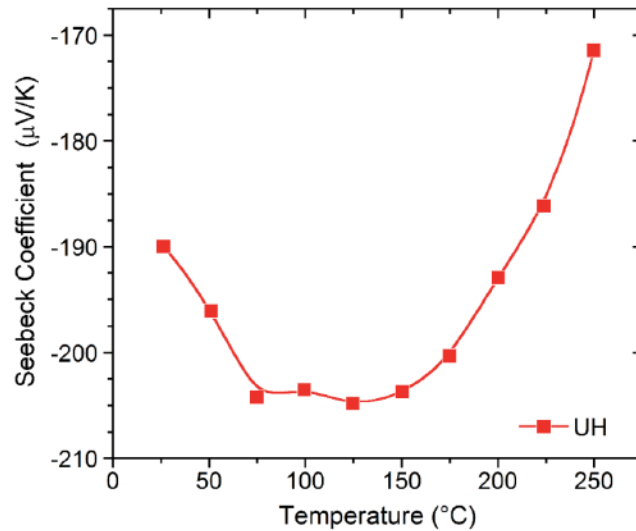


Figure 27. Seebeck coefficient α versus temperature for n-type bismuth telluride materials.

Figure 28 shows the electrical conductivity of the n-type BiTe materials measured from room temperature to 250°C. Conductivity is at a maximum of 100,000 S/m at room temperature and decreases with increasing temperature to a minimum of 58,000 S/m at 250°C.

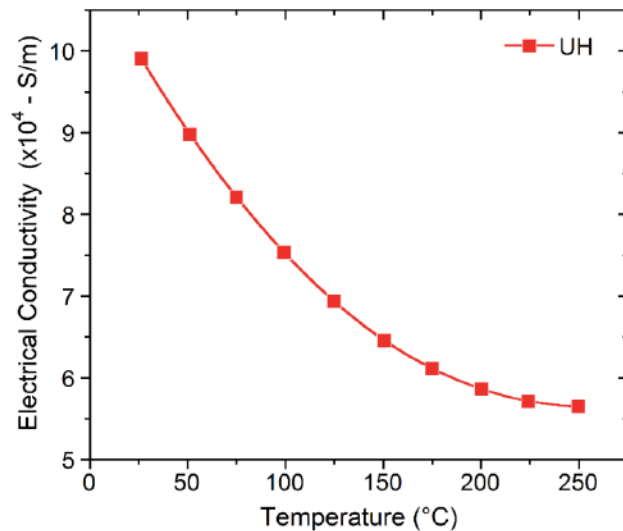


Figure 28. Electrical conductivity σ versus temperature for n-type bismuth telluride materials.

Figure 29 shows the thermal conductivity of the n-type BiTe materials measured from room temperature to 250°C. Conductivity reaches a minimum of 1.2 W/mK at 100°C.

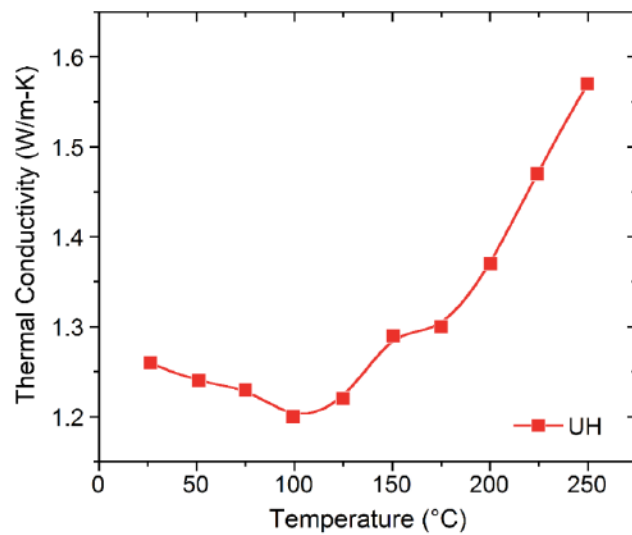


Figure 29. Thermal conductivity κ versus temperature for n-type bismuth telluride materials.

Figure 30 shows the ZT of the n-type BiTe materials measured from room temperature to 250°C. The materials have peak ZT of 0.97 at 75°C.

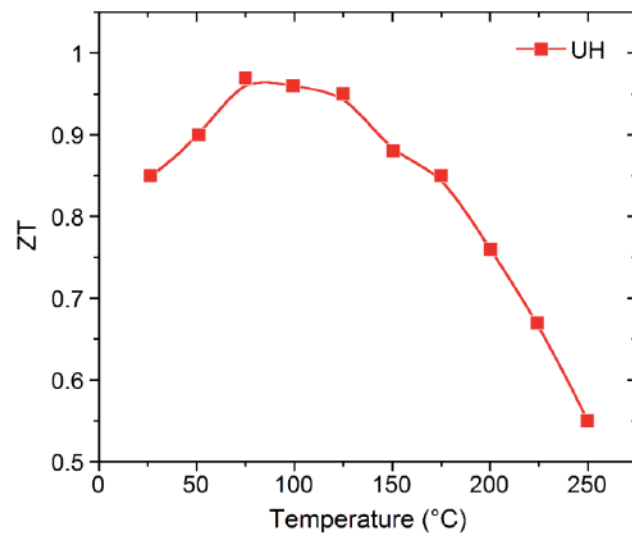


Figure 30. Energy dispersive X-ray spectroscopy, ZT, for n-type bismuth telluride materials.

Figure 31 shows the Seebeck coefficient of the p-type BiTe materials measured from room temperature to 250°C. The magnitude of the Seebeck coefficient increases from 193 $\mu\text{V/K}$ near room temperature to the peak of 218 $\mu\text{V/K}$ at 150°C.

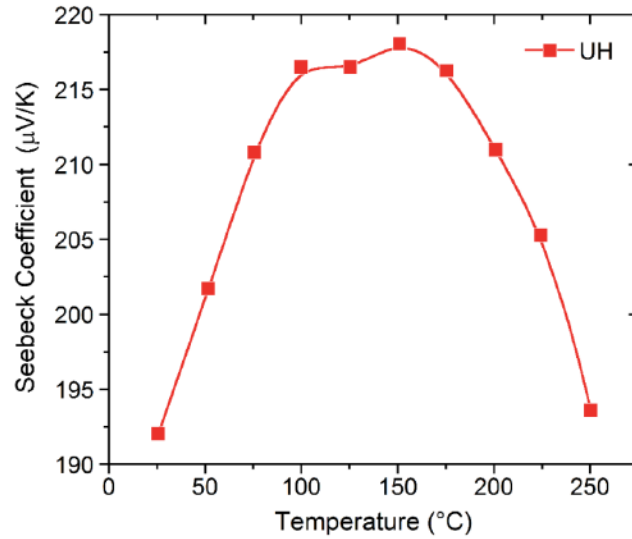


Figure 31. Seebeck coefficient α versus temperature for p-type bismuth telluride materials.

Figure 32 shows the electrical conductivity of the p-type BiTe materials measured from room temperature to 250°C. Conductivity is at a maximum of 100,000 S/m at room temperature and decreases with increasing temperature to a minimum of 41,000 S/m at 250°C.

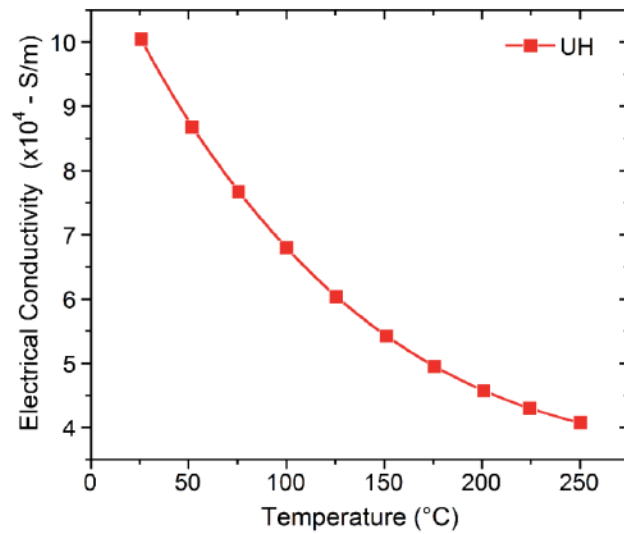


Figure 32. Electrical conductivity σ versus temperature for p-type bismuth telluride materials.

Figure 33 shows the thermal conductivity of the p-type BiTe materials measured from room temperature to 250°C. Conductivity reaches a minimum of 1.0 W/mK in the range of 100 to 150°C.

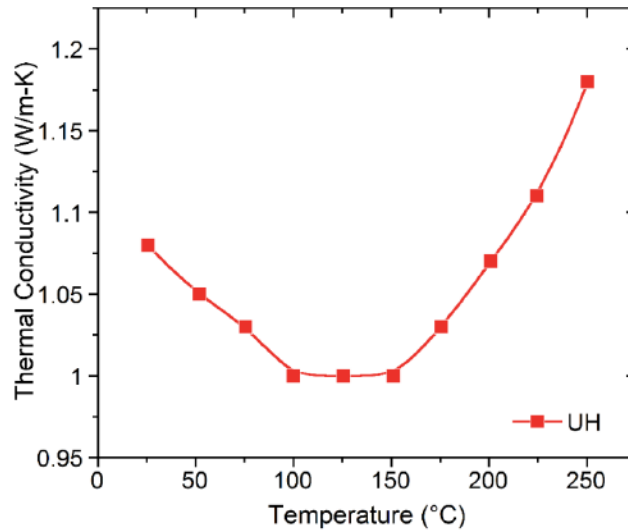


Figure 33. Thermal conductivity κ versus temperature for p-type bismuth telluride materials.

Figure 34 shows the ZT of the p-type BiTe materials measured from room temperature to 250°C. The materials have peak ZT near 1.2 at 100°C.

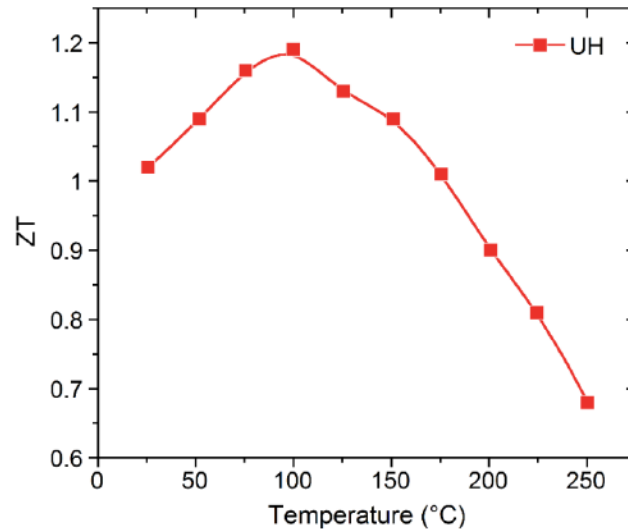


Figure 34. Energy dispersive X-ray spectroscopy, ZT, for p-type bismuth telluride materials.

4. CONCLUSIONS AND FUTURE WORK

BSU researchers selected the nanostructured bulk (nanobulk) HH and BiTe materials as the two TE material systems for this research.

The research team fabricated and characterized both nanobulk HH and BiTe materials and measured their TE properties. These two materials exhibit high ZT near or above 1 for the application temperature range of 30 to 600°C. In addition, their performance and reliability were well demonstrated at the device

and system level in several energy harvesting applications. The nanobulk HH materials have high ZT ideal for the heat source temperature range from 300 to 600°C, thus they are good candidates for power harvesting in NPPs both for the primary or secondary pipe loop systems where high-temperature waste heat is available. The nanobulk BiTe materials have high ZT ideal for the heat source temperature range from 100 to 250°C, thus they are good candidates for power harvesting in spent fuel storage facilities where low-temperature waste heat is available.

Future work of the project team will focus on further optimizing the performance of TE materials and studying the radiation effect on the two TE material systems—HH and BiTe materials. The project team will also start fabricating initial TE devices and test the performance of the devices under various heat source temperatures.

5. REFERENCES

- [1] NUREG/CR-6882, Assessment of Wireless Technologies and Their Application at Nuclear Facilities, Oak Ridge National Laboratory, July 2006.
- [2] Clayton, D.A., W.H.J. Andrews, and R. Lenarduzzi, *Power Harvesting Practices and Technology Gaps for Sensor Networks*, ORNL/TM-2012/442, Oak Ridge National Laboratory, September 2012.
- [3] Elsheikh, M.H., D. A. Shnawah, M.F.M. Sabri, S.B.M. Said, M.H. Hassan, M.B.A. Bashir, et al., A review on thermoelectric renewable energy: Principle parameters that affect their performance, *Renewable and Sustainable Energy*, Volume 30, February 2014, pp. 337-355.
- [4] Minnich, A.J., M.S. Dresselhaus, Z.F. Ren, and G. Chen, Bulk nanostructured thermoelectric materials: current research and future prospects, *Energy & Environmental Science*, Volume 2, Issue 5, 2009, pp. 466–479.
- [5] Radousky, H.B., and H. Liang, Energy harvesting: an integrated view of materials, devices and applications, *Nanotechnology*, Volume 23, Issue 50, 2012, 35 pp.
- [6] Yan, X.A., G. Joshi, W.S. Liu, Y.C. Lan, H. Wang, S. Lee, et al., Enhanced Thermoelectric Figure of Merit of p-Type Half-Heuslers, *Nano Letters*, Volume 11, Issue 2, 2011, pp. 556-560.
- [7] Yang, J., H.M. Li, T. Wu, W.Q. Zhang, L.D. Chen, and J.H. Yang, Evaluation of Half-Heusler Compounds as Thermoelectric Materials Based on the Calculated Electrical Transport Properties, *Advanced Functional Materials*, Volume 18, Issue 19, 2008, pp. 2880–2888.
- [8] Chen L., S. Gao, X. Zeng, A. Dehkordi, T. Tritt, and S. Poon, Uncovering High Thermoelectric Figure of Merit in (Hf, Zr)NiSn Half-Heusler Alloys, arXiv preprint arXiv:150507773, 2015.
- [9] Bos, J-W. G., and R.A. Downie, Half-heusler thermoelectrics: A complex class of materials, *Journal of Physics: Condensed Matter*, Volume 26, Issue 43, October 2014, 433201.
- [10] Sootsman, J.R., D.Y. Chung, and M.G. Kanatzidis, New and Old Concepts in Thermoelectric Materials, *Angewandte Chemie International Edition*, Volume 48, Issue 46, 2009, pp. 8616–8639.